

Anisotropic metamaterial with the ϵ -near- μ property in the entire angular domain enables broadband all-angle transmissions

Qihao Lv

Beijing Institute of Technology <https://orcid.org/0000-0003-3063-6563>

Cheng Jin (✉ jincheng@bit.edu.cn)

Beijing Institute of Technology

Binchao Zhang

Beijing Institute of Technology

Shuo Liu

State Key Laboratory of Millimeter Waves, Southeast University, Nanjing 210096, China

Tie Jun Cui

Southeast University <https://orcid.org/0000-0002-5862-1497>

Article

Keywords: metamaterials, communications, optics

Posted Date: June 21st, 2021

DOI: <https://doi.org/10.21203/rs.3.rs-602215/v1>

License:   This work is licensed under a Creative Commons Attribution 4.0 International License.

[Read Full License](#)

1 **Anisotropic metamaterial with the ϵ -near- μ property in the entire**
2 **angular domain enables broadband all-angle transmissions**

3 **Author Information**

4 **Affiliations**

5 **School of Information and Electronics, Beijing Institute of Technology, Beijing 100081, China**

6 Qihao Lv, Cheng Jin, & Binchao Zhang

7 **State Key Laboratory of Millimeter Waves, Southeast University, Nanjing 210096, China**

8 Shuo Liu & Tie Jun Cui

9 **Contributions**

10 Q. L. and C. J. conceived the concept and performed the analytical derivations and full-wave simulations;
11 B. Z. and S. L. fabricated the samples and performed the measurements; T. J. C. supervised the work. All
12 authors analyzed the data and prepared the manuscript.

13 **Corresponding author**

14 Correspondence to: Cheng Jin and Tie Jun Cui

15 **Abstract**

16 Epsilon-near-mu metamaterials play a significant role in many fields such as radar, communication, and
17 stealth technology, due to their ideal transmission responses. However, when electromagnetic (EM) waves
18 illuminate such metamaterials at large angles, undesired reflectance occurs that greatly restricts the
19 applications. Here, we propose a theoretical approach that can fundamentally eliminate the adverse effects
20 of the incident angle on the transmission response of an anisotropic ϵ -near- μ material by adjusting the
21 structural permittivity and permeability tensors. We take advantages of the nonresonance regions of electric
22 and magnetic resonators so that the material parameters can attain the desired values in a wide frequency

23 band. This allows us to design a nonreflective material with broadband all-angle transmissions from 0° to
24 almost 90° , which is further verified by experiments with good performance. This work opens up a new
25 route for the design of ultrawide-angle transmission-type metamaterials with high-efficiency and wideband
26 properties, reaching significant applications in antenna radomes.

27 **Introduction**

28 In the past decade, metamaterials have attracted tremendous attention at the frontier of physics, material,
29 and information sciences and engineering due to their peculiar capability of manipulating electromagnetic
30 (EM) waves¹. As a macroscopic composite of periodic or aperiodic structures, a metamaterial can realize
31 versatile fascinating phenomena, such as EM cloaking²⁻⁵, negative refraction⁶⁻¹³, perfect absorption¹⁴⁻¹⁶, and
32 superresolution imaging¹⁷⁻²⁰. The responses of metamaterials are commonly characterized by the effective
33 electric permittivity and magnetic permeability²¹, which are generally defined as tensors that depend on the
34 incident angle and operating frequency.

35 In the ε - μ domain, the parameters on the $\varepsilon = \mu$ line in both the right-handed ($\varepsilon > 0, \mu > 0$) and left-
36 handed ($\varepsilon < 0, \mu < 0$) material regions represent impedance-matching materials, which can achieve perfect
37 impedance matching with air. Based on this phenomenon, a variety of nonreflective structures have been
38 proposed in the past few years. Among the approaches, the quarter-wavelength transformer²² with refractive
39 index $n = \sqrt{n_s}$ perfectly matching that of air represents the simplest design. Despite its simple structure
40 design, it can only operate at a single frequency and at normal incidence, and its reflection is significantly
41 increased at a large incident angle. Moreover, inspired by the eyes of a moth, various graded-index (GRIN)
42 structures with antireflection responses were developed²³⁻²⁵. Multiple stacked layers are applied in these
43 GRIN structures, and the refractive index of each layer gradually decreases from the refractive index of the
44 substrate to that of air to achieve impedance matching with air. As a result, these structures can achieve
45 high transmission over a wide range of incident angles, although at the expense of excessive thickness and
46 fabrication difficulties. However, these GRIN structures suffer from high reflection at grazing incidence
47 angles. To achieve perfect impedance matching between the structure and air at grazing angles, a

48 nonreflective lens based on the Brewster effect was introduced²⁶. Under the theoretical guidance of the
49 Brewster effect, the proposed lens has achieved high-efficiency transmittance in the frequency band from
50 1 GHz to 16 GHz at an incident angle of 76.4° . However, only transverse magnetic (TM)-polarized EM
51 waves are allowed in such a Brewster-based structure.

52 In this article, we demonstrate an all-angle wideband transmission response by utilizing anisotropic
53 materials. Theoretical formulae are derived to reveal the relative permittivity and permeability tensors ($\bar{\epsilon}$
54 and $\bar{\mu}$) of the structure required for the angle-independent transparent response in the transverse electric
55 (TE) mode. As a proof of concept, we propose an ϵ -near- μ structure, whose relative permittivity and
56 permeability tensors are independently controlled by engineering an electric resonator and a magnetic
57 resonator, respectively. Moreover, the material parameters feature a flat frequency response in the
58 nonresonance region, and the electric and magnetic resonances are constructed on the two sides of the
59 desired operating band. Thus, the necessary conditions for $\bar{\epsilon}$ and $\bar{\mu}$ can be satisfied in the band of interest,
60 thereby achieving an ultrawide-angle transmission response in a wide frequency band.

61 **Results**

62 **Concept and theoretical analysis**

63 A material with all-angle transmission properties should be transparent to EM waves from all incident
64 angles, as conceptually illustrated in Fig. 1a. To achieve this goal, we begin our analysis with instances of
65 TM- and TE-polarized plane waves impinging on an isotropic material with an incident angle of θ , as
66 depicted in Fig. 1b. Here, the substrate is chosen as Rogers RO3003 with a relative permittivity (ϵ_r) of 3
67 and a relative permeability (μ_r) of 1. The reflection and transmission of a material are determined by
68 impedance matching between air and the material. The characteristic impedance of air at different incident
69 angles θ can be expressed as

$$70 \quad Z_{air}^{TM}(\theta) = \eta_0 \cos \theta \quad (1)$$

71 for TM incidence and

72
$$Z_{air}^{TE}(\theta) = \eta_0 / \cos \theta \quad (2)$$

73 for TE incidence, where η_0 is the free-space intrinsic impedance. The characteristic impedances of the
 74 substrate for TM and TE incidence are defined as Z_{sub}^{TM} and Z_{sub}^{TE} , respectively.

75 Following the boundary condition, the total reflection coefficients $R_{total}^{TM/TE}$ can be calculated as

76
$$R_{total}^{TM/TE} = \frac{R^{TM/TE}(1 - e^{-i2\beta d})}{1 - R^{TM/TE} e^{-i2\beta d}}, \quad (3)$$

77 where $R^{TM/TE} = (Z_{sub}^{TM/TE} - Z_{air}^{TM/TE}) / (Z_{sub}^{TM/TE} + Z_{air}^{TM/TE})$ represents the Fresnel reflection coefficient
 78 on the interface between the substrate and air; β denotes the propagation constant in the substrate; and d is
 79 the thickness of the substrate. By assuming Eq. (3) to be equal to zero, we can have two solutions: $R^{TM/TE} =$
 80 0 and $\beta d = k\pi$ ($k \in N_+$). However, as the propagation constant β is a linear function of frequency, the
 81 zero-reflection response obtained at $\beta d = k\pi$ is sensitive to frequency, which cannot be applied to achieve
 82 high-efficiency and wideband transmission performance. Thus, the wideband transmission response can
 83 only be realized when the characteristic impedance of air and the substrate matches, that is, $Z_{sub}^{TM/TE} =$
 84 $Z_{air}^{TM/TE}$, over a wide range of frequencies.

85 Fig. 1c gives the characteristic impedances of air and the substrate as a function of incident angle and
 86 frequency under TM-polarized plane wave illumination. The impedance of air intersects with that of the
 87 substrate for every frequency at the Brewster incident angle $\theta_{TM} = 60^\circ$, which ensures perfect transmission
 88 for the TM-polarized wave, while there is no intersection between the characteristic impedances of air and
 89 the substrate for the TE-polarized incident wave. The impedance difference significantly increases with
 90 increasing incident angle, as shown in Fig. 1d, which does not support zero reflection with a wideband
 91 characteristic. However, we can achieve the quasi-Brewster effect for the TE-polarized mode by matching
 92 the characteristic impedances of air and the designed structure. Specifically, perfect transmission
 93 performance for incident angles ranging from 0° to 90° can be obtained by applying such a quasi-Brewster
 94 effect to all incident angles, that is, by reducing the area of the red region marked in Fig. 1d. This provides
 95 us with a new method to design a zero-reflection structure with negligible angle dependence, as illustrated

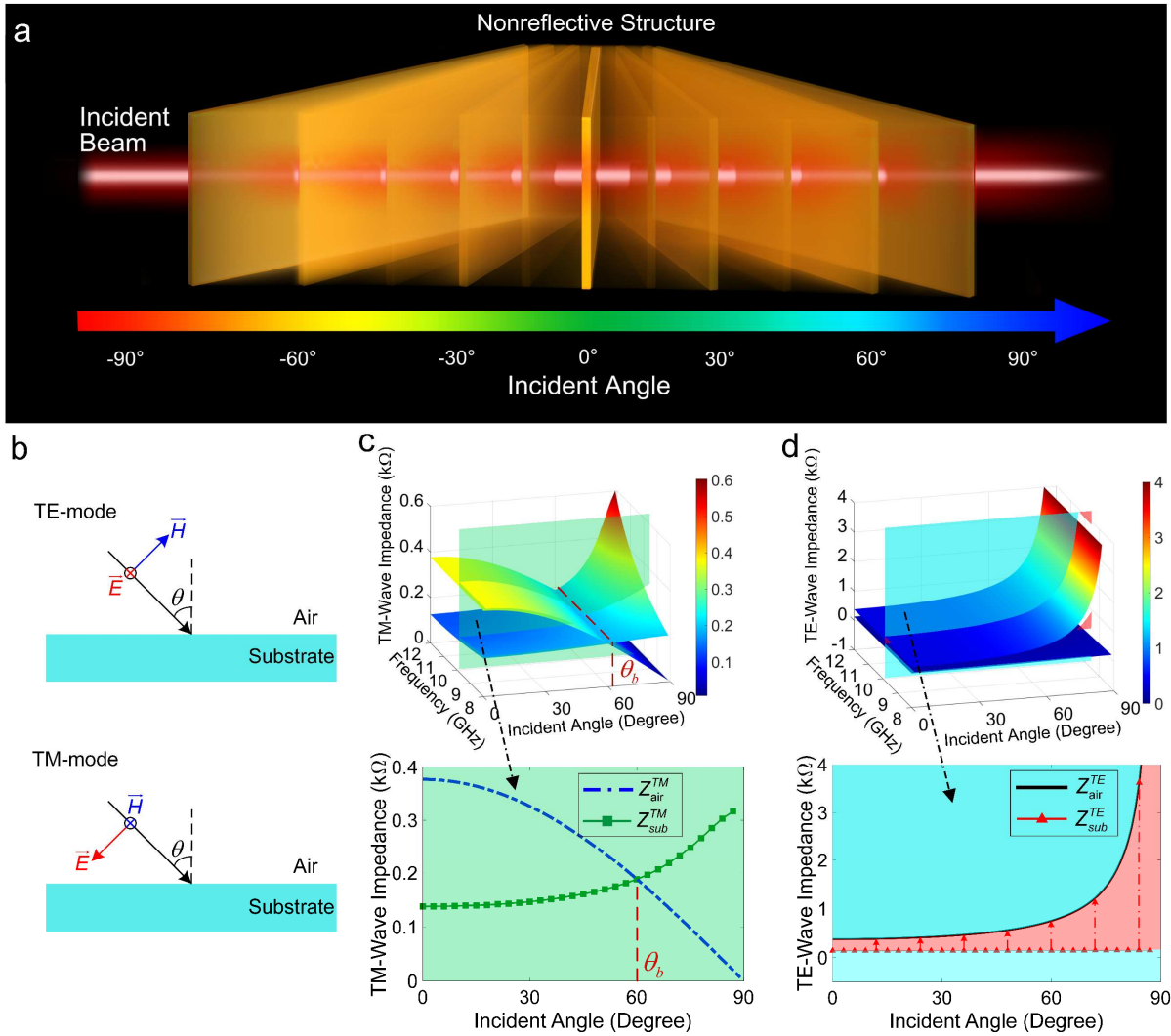


Fig. 1 Conceptual diagram of an all-angle nonreflective material and cases of EM waves illuminating an isotropic substrate with different incident angles. **a** Conceptual diagram of the designed nonreflective structure. **b** Propagation path of the incident wave from air to the substrate for TE and TM modes. **c** Impedances of air and the substrate versus incident angle and frequency for the TM mode and **(d)** TE mode, and cross-sections of their impedances at 10 GHz are given at the bottom of each figure.

96 in Fig. 1a.

97 Previous analysis has confirmed that achieving a high-efficiency transmission response in the entire
 98 angular domain with naturally occurring materials is impossible. Therefore, we consider uniaxial materials
 99 with anisotropic properties, whose relative permittivity and permeability tensors are functions of frequency
 100 and expressed as

101
$$\bar{\epsilon}(\omega) = \begin{bmatrix} \epsilon_t(\omega)\epsilon_0 & 0 & 0 \\ 0 & \epsilon_t(\omega)\epsilon_0 & 0 \\ 0 & 0 & \epsilon_n(\omega)\epsilon_0 \end{bmatrix} \quad (4)$$

102 and

103
$$\bar{\mu}(\omega) = \begin{bmatrix} \mu_t(\omega)\mu_0 & 0 & 0 \\ 0 & \mu_t(\omega)\mu_0 & 0 \\ 0 & 0 & \mu_n(\omega)\mu_0 \end{bmatrix}, \quad (5)$$

104 respectively. To simplify the analysis process, all the elements in the relative permittivity and permeability
 105 tensors are assumed to be real numbers. The subscript t represents the tangential components in the x - and
 106 y -directions, and n denotes the normal component in the z -direction.

107 For simplicity, we assume a plane wave in the xz -plane and illuminates on the uniaxial material at an
 108 angle θ . According to a previous work²⁷, the characteristic impedance of the uniaxial material for TE-
 109 polarized incidence can be expressed as

110
$$Z_{um}^{TE}(\theta, \omega) = \frac{\eta_0}{\sqrt{\frac{\epsilon_t(\omega)}{\mu_t(\omega)} \frac{\sin^2 \theta}{\mu_t(\omega)\mu_n(\omega)}}}. \quad (6)$$

111 For the characteristic impedance of the uniaxial material to be equal that of air at all incident angles, they
 112 must satisfy the following conditions: 1) the characteristic impedances of the uniaxial material and air are
 113 the same at normal incidence; 2) the slope of the characteristic impedance curve of the material equals that
 114 of air at all incident angles. These conditions lead to the following equations:

115
$$\begin{cases} Z_{um}^{TE}(0, \omega) = Z_{air}^{TE}(0, \omega) \\ \left. \frac{dZ_{um}^{TE}(\theta, \omega)}{d\theta} = \frac{dZ_{air}^{TE}(\theta, \omega)}{d\theta} \right|_{\theta \in (0, \frac{\pi}{2})} \end{cases} \Rightarrow \begin{cases} \epsilon_t(\omega) = \mu_t(\omega) \\ \mu_t(\omega)\mu_n(\omega) = 1 \end{cases} \quad (7)$$

116 Furthermore, to more intuitively reveal the effect of the above parameters (ϵ_t , μ_t , and μ_n) on the
 117 performance of the uniaxial material, we substitute Eq. (1) and Eq. (6) into the Fresnel reflection coefficient
 118 R^{TE} , yielding a reflection coefficient equation of

119
$$R^{TE}(\theta, \omega) = \frac{Z_{um}^{TE}(\theta, \omega) - Z_{air}^{TE}(\theta, \omega)}{Z_{um}^{TE}(\theta, \omega) + Z_{air}^{TE}(\theta, \omega)} = \frac{\cos \theta - \sqrt{\frac{\epsilon_t(\omega)}{\mu_t(\omega)} \frac{\sin^2 \theta}{\mu_t(\omega)\mu_n(\omega)}}}{\cos \theta + \sqrt{\frac{\epsilon_t(\omega)}{\mu_t(\omega)} \frac{\sin^2 \theta}{\mu_t(\omega)\mu_n(\omega)}}}. \quad (8)$$

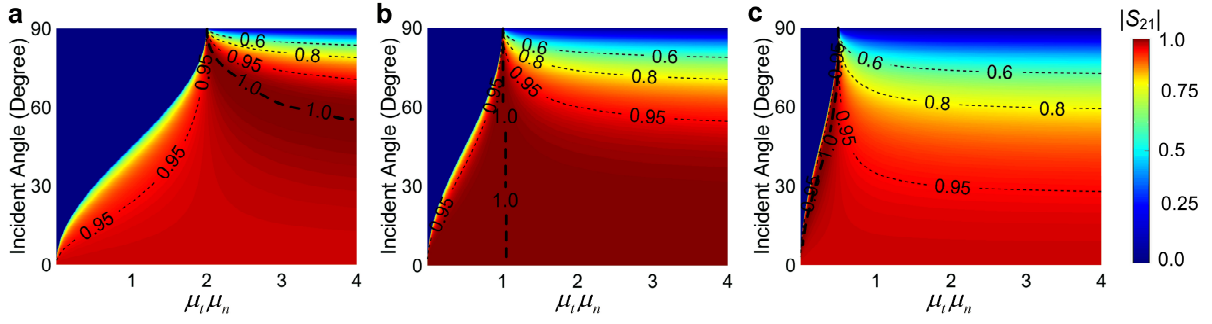


Fig. 2 Simulated transmission coefficients versus the incident angle and the product $\mu_t\mu_n$ under cases of (a) $\varepsilon_t(\omega) = 0.5 * \mu_t(\omega)$, (b) $\varepsilon_t(\omega) = \mu_t(\omega)$, and (c) $\varepsilon_t(\omega) = 2 * \mu_t(\omega)$.

120 The transmission coefficients of the uniaxial material for TE-polarized waves are presented in Fig. 2
 121 as a function of $\mu_t\mu_n$ and incident angle. According to these figures, unity transmission with zero angular
 122 dependence can only be achieved when $\varepsilon_t(\omega) = \mu_t(\omega)$ and $\mu_t(\omega)\mu_n(\omega) = 1$ are simultaneously satisfied
 123 (see Fig. 2b), in accordance with Eq. (7). However, for the other cases with $\varepsilon_t(\omega) \neq \mu_t(\omega)$, the
 124 transmission coefficient experiences large variations with the incident angle.

125 Design of an angle-independent transmission material

126 According to the Drude-Lorentzian model²⁸, the permittivity of the structure experiences rapid changes
 127 with frequency at the resonance of an electric resonator but varies smoothly away from the resonance².
 128 Notably, its permittivity is higher than that of the substrate in the high-frequency nonresonance region and
 129 is lower in the low-frequency nonresonance region. Similarly, a magnetic resonator has the same effect on
 130 the permeability of the structure. Therefore, the permittivity can be reduced at higher frequencies than the
 131 electric resonant mode, and the permeability can be increased at lower frequencies than the magnetic
 132 resonant mode, which leads to equality between the relative permittivity and permeability over a wide
 133 frequency band. This allows us to design an ε -near- μ (ENM) structure with a broadband characteristic.

134 As a proof of concept, an electric resonator and a magnetic resonator are introduced into a substrate
 135 with a relative permittivity of 3 to independently manage its relative permittivity and permeability. The
 136 structure is simulated in ANSYS HFSS with periodic boundary conditions, and a TE-polarized incident

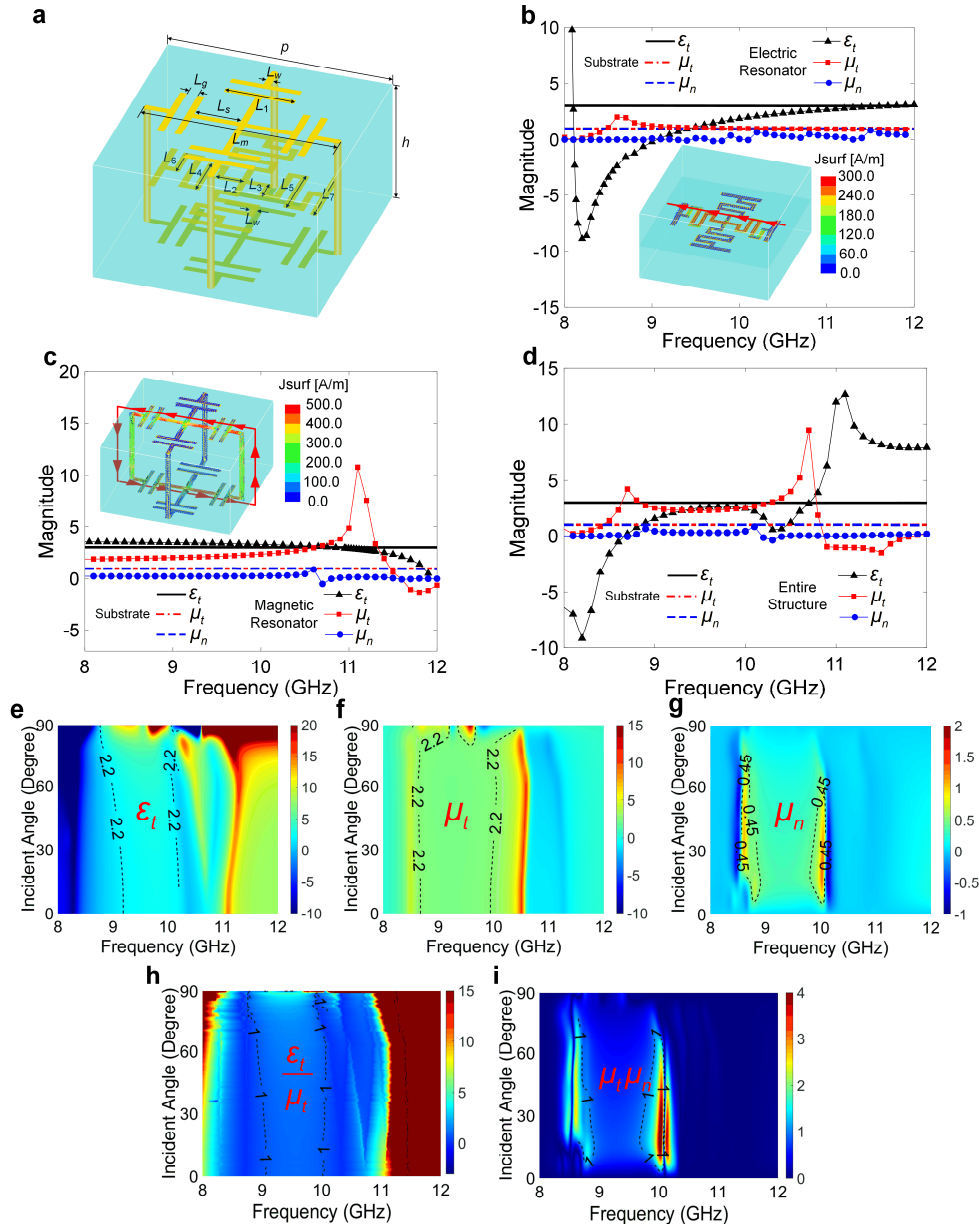


Fig. 3 Unit cell of ENM structure and influence of electric and magnetic resonators on material parameters. **a** Configuration of the final design ($p = 6.4$, $h = 3.6$, $L_m = 5.4$, $L_s = 1.3$, $L_g = 0.3$, $L_w = 0.2$, $L_1 = 2.0$, $L_2 = 0.7$, $L_3 = 0.5$, $L_4 = 1.2$, $L_5 = 1.5$, $L_6 = 0.8$, and $L_7 = 2.0$, all dimensions are in mm). **b** Current distributions of the electric resonator and its impact on material parameters. **c** Current distributions of the magnetic resonator and its influence on material parameters. **d** Material parameters of the final design. Extracted structural parameters of the final design: **(e)** tangential permittivity ϵ_t , **(f)** tangential permeability μ_t , and **(g)** normal permeability μ_n . Variables **(h)** ϵ_t/μ_t and **(i)** μ_t/μ_n are plotted against the frequency and incident angle; both are close to one in the desired frequency band, satisfying the required conditions in Eq. (7).

137 wave is contained in the xz -plane, whose electric field is along the y -axis. The unit cell of the ENM structure

138 is constructed by combining the electric resonator and the magnetic resonator in a three-layer configuration,
139 as displayed in Fig. 3a, in which the electric resonator is located in the middle layer and the magnetic
140 resonator is located in the bottom and top layers. Detailed parameters of the material are given in the caption
141 of Fig. 3. As shown in Fig. 3b, a cross-shaped metallic strip as an electric resonator is printed on the center
142 layer of the substrate, and induced currents along the $-y$ -axis stimulate a variation in the tangential relative
143 permittivity. The metal strip is designed to resonate at approximately 8 GHz, and the tangential relative
144 permittivity exhibits a flat frequency response with a value of 2 in the nonresonance region from 9 GHz to
145 10 GHz. The tangential and normal components of the relative permeability are hardly affected.

146 The magnetic resonator is realized by a loop resonator, which is printed on the top and bottom layers
147 of the substrate and connected by metallic vias, as depicted in Fig. 3b. The induced currents flow
148 counterclockwise along the magnetic resonator, generating a magnetic effect at 11 GHz, whose resonant
149 frequency is determined by the circumference of the loop resonator. The tangential permeability is increased
150 from unity to nearly 2.0 from 9 GHz to 10 GHz, while the structural permittivity remains almost unchanged.

151 Fig. 3d depicts the extracted material parameters (ϵ_t , μ_t , and μ_n) of the final design under normal
152 incidence. Furthermore, Fig. 3e-3i shows the extracted material parameters of the structure as a function of
153 incident angle and frequency. The structural parameters exhibit a stable angular response from 9 GHz to 10
154 GHz. In the band of interest, the tangential relative permittivity of approximately 2.2 is close to the
155 tangential relative permeability, while the normal permeability is approximately 0.45. In addition, we plot
156 the variables ϵ_t/μ_t and $\mu_t\mu_n$ with respect to the frequency and incident angle in Fig. 3g and Fig. 3h,
157 respectively. The tangential relative permittivity and permeability are almost the same, and the product of
158 the tangential and normal relative permeabilities is close to unity over a wide frequency band, which is
159 consistent with Eq. (7).

160 To further clarify the ultrawide-angle broadband transmission characteristic of our proposed ENM
161 structure, full-wave simulations of TE-mode EM waves with different incident angles are carried out in the
162 HFSS simulator. Fig. 4 shows the E -field distributions at three representative frequencies of 9 GHz, 9.5

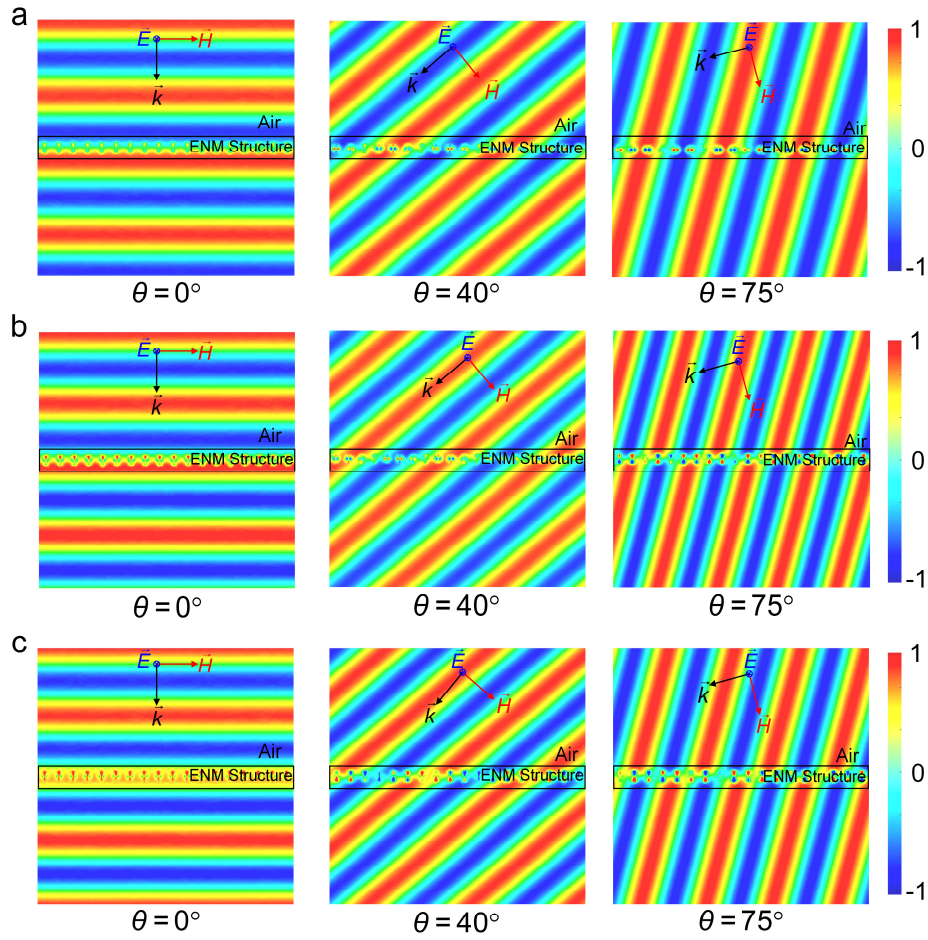


Fig. 4 Simulated E -field distributions when TE-polarized EM waves pass through the proposed ENM structure under different incident angles θ at three representative frequencies of (a) 9 GHz, (b) 9.5 GHz, and (c) 10 GHz in the operating band.

163 GHz, and 10 GHz in the operating band under different incident angles of 0° , 40° , and 75° . We observe
 164 that the existence of the proposed ENM structure does not change the propagation direction of the EM
 165 waves at ultrawide incident angles. In addition, the amplitudes of the transmitted waves for all three incident
 166 angles are almost the same as those of the incident waves, while their phase shifts can be negligible due to
 167 the low refractive index of the structure²⁹.

168 To experimentally demonstrate the proposed concept, we fabricate a prototype composed of 37×37
 169 elements with an overall size of $236.8 \text{ mm} \times 236.8 \text{ mm} \times 3.6 \text{ mm}$, as shown in Fig. 5a. The transmission
 170 performance of the fabricated sample is experimentally characterized in an anechoic chamber using a vector

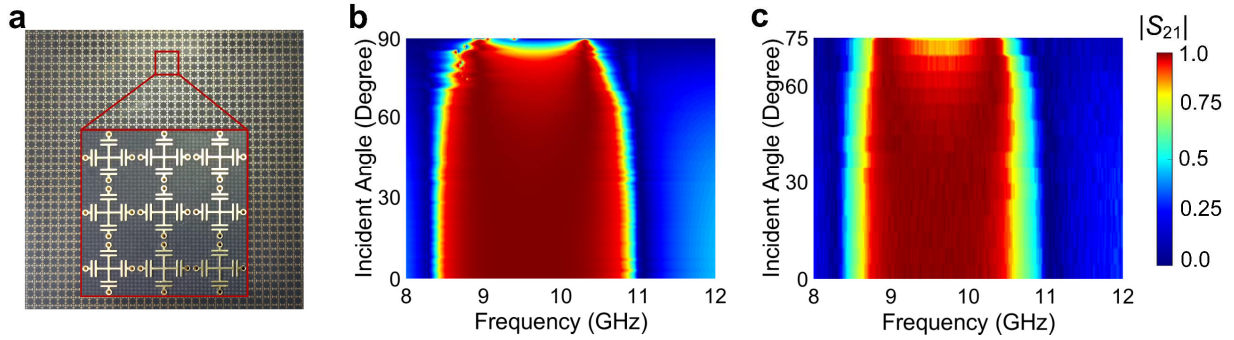


Fig. 5 Measured results at microwave frequencies. **a** Fabricated sample with 37*37 elements. **b** Simulated and **(c)** measured transmission spectra of the designed ENM structure. The sample is measured from 0° to 75° with a step of 5° due to the limitations of the measurement setup. In the measured spectra, the results measured at each sampling incident angle are utilized to signify the results of the five nearby degrees.

171 network analyzer (see Methods for the detailed measurement setup). Note that due to experimental
 172 limitations, the transmission coefficients of the sample are tested at incident angles from 0° to 75° with a
 173 step of 5°. The simulated and measured transmission coefficients are shown in Fig. 5b and c, respectively,
 174 which are in good agreement. Both the simulated and measured results show that the designed ENM
 175 structure exhibits high-efficiency transmission over a broad frequency band (9.0-10.2 GHz) and wide
 176 incident angles (0-75°). This proves that the material parameters required by Eq. (7) in a broad operation
 177 band have the potential to achieve angle-independent broadband transmission performance.

178 Discussion

179 In this work, we propose a theory to enhance the transmittance of metamaterials under oblique incidence
 180 over a wide range from normal to extreme grazing angles. We achieve this goal by matching the
 181 characteristic impedances of the material and air at all incident angles. Based on theoretical analysis, we
 182 discover for the first time that anisotropic ENM metamaterials with equal tangential relative permittivity
 183 and permeability ($\epsilon_t = \mu_t$) and a product of the tangential and normal relative permeabilities of unity
 184 ($\mu_t \mu_n = 1$) can ideally eliminate the impact of the incident angle on their transmission. To implement such
 185 an anisotropic metamaterial, we engineer electric and magnetic resonances on the two sides of the operating
 186 band to endow the structural permittivity and permeability with the theoretically predicted values. Since

187 the working band is located in the nonresonance region, the permittivity and permeability of the structure
188 feature a flat frequency response, which helps achieve broadband transmission performance. Experimental
189 results have verified that the proposed ENM material can maintain high transmission under large oblique
190 incidence. The promising performance of the designed ENM structure also suggests that our proposed
191 theory has potential applications in conformal radomes, which urgently require an ultrawide angular
192 response.

193 **Methods**

194 **Sample fabrication**

195 The designed ENM structure is fabricated by using PCB technology. The sample is composed of three
196 metal layers and two substrate layers. The top and middle metal layers are printed on one substrate layer by
197 using vacuum etching technology, while the bottom metal layer is printed on the backside surface of another
198 substrate layer. Then, we use lamination technology to combine these two substrate layers together. Finally,
199 vertical via holes covered with metal are fabricated throughout the entire structure to connect the upper and
200 lower metal layers.

201 **Measurement setup**

202 The transmission spectra of the fabricated ENM structure are measured with the help of the free-space
203 method in a microwave anechoic chamber. The sample is embedded in the window of an absorbing screen.
204 The transmitting and receiving antennas are coaxially aligned on the two sides of the screen, and the surface
205 of the screen is orthogonal to the propagation direction of the EM wave. The distances between the device
206 under test and both antennas are set to be 3 meters to satisfy the far-field condition. The vector network
207 analyzer is connected to both antennas through $50\ \Omega$ coaxial cables to measure the transmission response
208 of the fabricated sample. Due to the limitations of the measurement setup, the angular response of the ENM
209 structure is tested when the absorbing screen is rotated from 0° to 75° with a step of 5° . The measured
210 results at each incident angle are first terminated in the time domain to eliminate environmental interference

211 by measuring the case with a bare perfect electric conductor (PEC) board of the same size and then
212 normalized to the reference case of the air window.

213 **Data Availability**

214 The data that support the findings of this study are available on request from the corresponding authors.

215 **References**

- 216 1. Overvelde, J. T. B., Jong, T. A. D., Shevchenko, Y., Becerra, S. A., Whitesides, G. M., Weaver, J. C.,
217 Hoberman, C. & Bertoldi, K. A three-dimensional actuated origami-inspired transformable
218 metamaterial with multiple degrees. *Nat. Commun.* **7**, 10929 (2016).
- 219 2. Leonhardt, U. Optical conformal mapping. *Science* **312**, 1777–1780 (2006).
- 220 3. Pendry, J. B., Schurig, D. & Smith, D. R. Controlling electromagnetic fields. *Science* **312**, 1780–1782
221 (2006).
- 222 4. Alù, A. & Engheta, N. Achieving transparency with plasmonic and metamaterial coatings. *Phys. Rev.*
223 *E* **72**, 016623 (2005).
- 224 5. Schurig, D. et al. Metamaterial electromagnetic cloak at microwave frequencies. *Science* **314**, 977–980
225 (2006).
- 226 6. Soukoulis, C. M., Linden, S. & Wegener, M. Negative refractive index at optical wavelengths. *Science*
227 **315**, 47–49 (2007).
- 228 7. Smith, D. R., Padilla, W. J., Vier, D. C., Nemat-Nasser, S. C. & Schultz, S. Composite Medium with
229 simultaneously negative permeability and permittivity. *Phys. Rev. Lett.* **84**, 4184 (2000).
- 230 8. Smith, D. R., & Schurig, D. Electromagnetic wave propagation in media with indefinite permittivity and
231 permeability tensors. *Phys. Rev. Lett.* **90**, 077405 (2003).
- 232 9. Shelby, R. A., Smith, D. R. & Schultz, S. Experimental verification of a negative index of refraction.
233 *Science* **292**, 77 (2001).

- 234 10. Veselago, V. G. The electrodynamics of substances with simultaneously negative value of ϵ and μ . *Sov.*
235 *Phys. Usp.* **10**, 509 (1968).
- 236 11. Pendry, J. B. Negative refraction makes a perfect lens. *Phys. Rev. Lett.* **85**, 3966–3969 (2000).
- 237 12. Valentine, J. et al. Three-dimensional optical metamaterial with a negative refractive index. *Nature* **455**,
238 376–380 (2008).
- 239 13. Zhang, S., Fan, W., Panoiu, N. C., Malloy, K. J., Osgood, R. M. & Brueck, S. R. J. Experimental
240 demonstration of near-infrared negative-index metamaterials. *Phys. Rev. Lett.* **95**, 137404 (2005).
- 241 14. Landy, N. I., Sajuyigbe, S., Mock, J. J., Smith, D. R. & Padilla, W. J. Perfect metamaterial absorber.
242 *Phys. Rev. Lett.* **100**, 207402 (2008).
- 243 15. Liu, X., Tyler, T., Starr, T., Starr, A. F., Jokerst, N. M. & Padilla, W. J. Taming the blackbody with
244 infrared metamaterials as selective thermal emitters. *Phys. Rev. Lett.* **107**, 045901 (2011).
- 245 16. Liu, N., Mesch, M., Weiss, T., Hentschel, M. & Giessen, H. Infrared perfect absorber and its application
246 as plasmonic sensor. *Nano Lett.* **10**, 2342 (2010).
- 247 17. Engheta, N. & Ziolkowski, R. W. *Metamaterials: Physics and Engineering Explorations* (IEEE-Wiley,
248 New York, 2006).
- 249 18. Zhang, X. & Liu, Z. W. Superlenses to overcome the diffraction limit. *Nat. Mater.* **7**, 435–441 (2008).
- 250 19. Dubois, M. et al. Time-driven super oscillations with negative refraction. *Phys. Rev. Lett.* **114**, 013902
251 (2015).
- 252 20. Lee, H., Oh, J. H., Seung, H. M., Cho, S. H. & Kim, Y. Y. Extreme stiffness hyperbolic elastic
253 metamaterial for total transmission subwavelength imaging. *Sci. Rep.* **6**, 24026 (2016).
- 254 21. Cui, T. J., Smith, D. R. & Liu, R. P. *Metamaterials: Theory, Design and Applications* (Springer, 2010).
- 255 22. Cheng, D. K. *Field and Wave Electromagnetics*, 2nd ed. (Addison-Wesley, Boston, MA, 1989).

- 256 23. Clapham, P. B. & Hutley, M. C. Reduction of lens reflexion by the ‘moth eye’ principle. *Nature* **244**,
257 5414 (1973).
- 258 24. H. A. Macleod, *Thin-Film Optical Filters*. (Boca Raton, FL, USA: CRC Press, 2001).
- 259 25. Tao, Z., Jiang, W., Ma, H. & Cui, T. High-gain and high-efficiency GRIN metamaterial lens antenna
260 with uniform amplitude and phase distributions on aperture. *IEEE Trans. Antennas Propag.* **66**, 16-22
261 (2018).
- 262 26. Huang, H & Shen, Z. X. Brewster lens with perfect wave refraction. *IEEE Trans. Antennas Propag.*
263 **68**, 6204-6213 (2020).
- 264 27. He, Y. & Eleftheriades, G. V. Anisotropic metamaterial as an antireflection layer at extreme angles.
265 *IEEE Trans. Antennas Propag.* **65**, 4102-4114 (2017).
- 266 28. Dani, K. M., Ku, Z. Y., Upadhyaya, P. C., Prasankumar, R. P., Brueck, S. R. J. & Taylor, A. J.
267 Subpicosecond optical switching with a negative index metamaterial. *Nano Lett.* **9**, 3565–3569 (2009).
- 268 29. Wang, C., Zhu, Z., Cui, W., Yang, Y., Ran, L. & Ye, D. All-angle brewster effect observed on a
269 terahertz metasurface. *Appl. Phys. Lett.* **114**, 191902 (2019).

270 **Acknowledgments**

271 This work was supported by the National Natural Science Foundation of China under grant 61871036, the
272 Open Project of the State Key Laboratory of Millimeter Waves under grant K202018, and the National Key
273 Research and Development Program of China under grants 2017YFA0700201, 2017YFA0700202, and
274 2017YFA0700203.

275 **Author contributions**

276 Q. L. and C. J. conceived the concept and performed the analytical derivations and full-wave simulations;
277 B. Z. and S. L. fabricated the samples and performed the measurements; T. J. C. supervised the work. All
278 authors analyzed the data and prepared the manuscript.